Noname manuscript No.
(will be inserted by the editor)

The lightning method for the heat equation

Hunter La Croix · Alan E. Lindsay

June 27, 2025

Abstract This paper introduces a new method for solving the planar heat equation based on the Lightning Method. The lightning method is a recent development in the numerical solution of linear PDEs which expresses solutions using sums of polynomials and rational functions, or more generally as sums of fundamental solutions. The method is particularly well suited to handle domains with sharp corners where solution singularities are present. Boundary conditions are formed on a set of collocation points which is then solved as an overdetermined linear system. The approach of the present work is to utilize the Laplace transform to obtain a modified Helmholtz equation which is solved by an application of the lightning method. The numerical inversion of the Laplace transform is then performed by means of Talbot integration. Our validation of the method against existing results and multiple challenging test problems shows the method attains spectral accuracy with root-exponential convergence while being robust across a wide range of time intervals and adaptable to a variety of geometric scenarios.

Keywords Lightning Method, Laplace Transform, Diffusion Equation, Fundamental Solutions, Least Squared Solution.

1 Introduction.

The purpose of this work is to present a new approach for the numerical solution of the planar heat equation by means of *the lightning method* (LM), recently introduced by Gopal and Trefethen [17]. The specific problem of interest is the parabolic partial differential equation

$$\frac{\partial u}{\partial t} = D\Delta u, \qquad (x,t) \in \mathbb{R}^2 \setminus \Omega \times (0,\infty); \tag{1a}$$

$$u = f(x), \qquad (x,t) \in \partial\Omega \times (0,\infty); \tag{1b}$$

$$u = u_0(x), \qquad (x,t) \in \mathbb{R}^2 \setminus \Omega \times (t=0). \tag{1c}$$

where Ω is a collection of N_B polygonal absorbing bodies ($\Omega := \cup_{k=1}^{N_B} \Omega_k$). A schematic of the geometric configuration is shown in Fig. 1.

In this work, we show that by combining the Laplace transform with the lightning method, a rapid, robust, accurate and easy to implement numerical solution to (1) can be developed. The derived method is spectrally accurate (root-exponential convergence) and resolves corner singularities of (1) inherent to polygonal geometries. On a variety of challenging test cases, we will demonstrate our method is routinely capable of attaining relative solution accuracies of order $\mathcal{O}(10^{-10})$, consistent with other implementations of the lightning method [2,16].

Dept. of Applied and Computational Math & Statistics, University of Notre Dame, Notre Dame, Indiana, 46656, USA; e-mail: e-mail: hlacroix@nd.edu

Dept. of Applied and Computational Math & Statistics, University of Notre Dame, Notre Dame, Indiana, 46656, USA; e-mail: a.lindsay@nd.edu

Address(es) of author(s) should be given

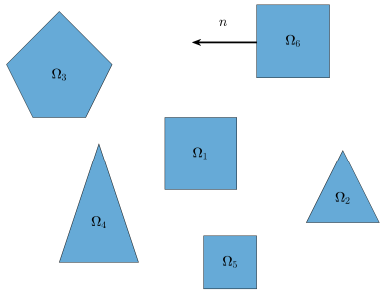

Fig. 1: Schematic of the external geometry $\mathbb{R}^2 \setminus \Omega$ on which the parabolic system (1) is solved. The set of N_B polygonal bodies is $\Omega := \cup_{k=1}^{N_B} \Omega_k$ and n is the outward facing normal vector to $\partial\Omega$.

The lightning method was originally developed in [17,16] for the solution of Laplace and Helmholtz equations. It is in essence a complex variable technique that expresses the solution of elliptic PDEs as a rational function. It has since been extended to solve problems for potential flow [2] and Stokes flow [7]. It is able to accurately resolve solutions of linear PDEs with corners which present challenges to traditional stencil based methods due to their solution singularities.

Due to the fundamental importance of (1) in many disparate applications, significant efforts have gone in to numerical techniques to approximate its solution. These including boundary integral methods [8,14,27, 10], Volterra integral equations [21,26,44] and various transform methods [18,30], Abel transforms [40,47, 50,11,24]. Monte-Carlo methods are an important companion to deterministic methods that cast solutions of (1) as a probability distribution that can be sampled by particle systems [39,19,23,45,42,9]. While slow to converge, Monte Carlo methods have no issues dealing with difficulties inherent to stencil solution methods such as corner singularities. However, an advantage of continuous PDE methods is that the density $u(x,t)$ is obtained everywhere which yields much more detail on the trajectories of diffusing particles. Since discrete and continuous methods for the solution of (1) each have their inherent advantages and disadvantages, it is valuable to advance all feasible methods for its solution.

A particular motivation of the present study is the solution of diffusive capture problems in cellular biology [32,35,38,9,29,6,42]. A specific quantity of interest is the time taken for a diffusing molecule initialized at x_0 to reach the target set $\partial\Omega$, the so-called *first passage time* (FPT) distribution [28]. This involves solving (1) with the boundary condition $f = 0$ and the initial condition $u_0(x) = \delta(x - x_0)$. The main quantities of interest in this setting are

$$j(t) = \int_{\partial\Omega} D\frac{\partial u}{\partial n}\, ds, \qquad c(t) = \int_0^t j(\eta)\, d\eta. \tag{2}$$

where $\partial u/\partial n := n \cdot \nabla u$ is the outward facing normal derivative. In terms of particle diffusion, this quantity is encoded by the first arrival time τ where

$$\tau = \inf_{0<t<\infty}\{x(t) \in \partial\Omega\}; \qquad dx = \sqrt{2D}\, dW_t, \qquad x(0) = x_0; \tag{3a}$$

and W_t is the Wiener process. The probabilistic quantities associated to this process are then

$$\mathbb{P}[\tau = t] = j(t), \qquad \mathbb{P}[\tau < t] = c(t). \tag{3b}$$

In our validation of the numerical solution to (1), particle-based solutions [9] will provide a highly non-trivial but low-fidelity validation.

In the present work, we utilize the Laplace transform which reduces (1) to a modified Helmholtz equation. We then propose and implement a lighting method to solve this elliptic PDE, followed by an inversion of the Laplace transform. The inverse transform is accomplished by means of Talbot integration [49,46,

12] a highly optimized and rapid method for evaluation of the Bromwich integral. This Laplace transform approach has been successfully demonstrated on parabolic problems in unbounded domains [37,9,34,10] with notable advantages being its ability to bypass the time-step limitations of traditional integrators and achieve accuracy close to machine precision.

The key enabler in this approach is a rapid and accurate method for solving the modified Helmholtz equation associated with the transform problem. In recent work [10], the second author and collaborators used a boundary integral approach for this purpose which expressed the solution of the modified Helmholtz equation in terms of appropriate layer potentials. In the present work, we adapt the Lightning method for this purpose [17]. The LM expresses the solution as a series of rational functions which solve the homogeneous equation exactly. The coefficients of this series are calculated from the least squared solution of an overdetermined linear system formed at a collocation grid along $\partial\Omega$. The Lightning method has been applied to Laplace problems, whose simplicity has allowed for theoretical analysis such as proof of root-exponential convergence and optimal clustering of poles [16,20]. Previous works have demonstrated the efficacy of the LM for the Helmholtz equation [17,15], however, its complexity when compared to the Laplace problem has hindered theoretical results. Thus, our contribution is a computational demonstration that LM solution of the Modified Helmholtz equation (and consequently the heat equation) is effective.

The outline of the paper is as follows. In Sec. 2 we describe our numerical approach, including implementation details of the LM for the modified Helmholtz equation and application of Talbot integration to obtain the inverse Laplace transform. In Sec. 3, we will describe two alternative solutions, the kinetic Monte Carlo method and matched asymptotic expansions, that will be used to validate the results of the LM. In Sec. 4 we demonstrate our method on a variety of test problems. We demonstrate the method on domains with single or multiple absorbers, and varied boundary and initial conditions. Finally, we discuss potential extensions and avenues for future research arising from this study.

2 Numerical methods.

In this section, we outline our approach to determine the numerical solution of (1). The method we describe leverages complex variables to solve linear PDEs in the plane. The solution $u = u(z,t)$ where $z \in \mathbb{C}$, and $x = (\mathrm{Re}(z), \mathrm{Im}(z))$ is the independent spatial variable. The Laplace transform for $s \in \mathbb{C}$ is defined as the integral

$$\hat{u}(z;s) = \mathcal{L}(u) = \int_{t=0}^{\infty} u(z,t)e^{-st}dt. \tag{4}$$

Applying (4) to equation (1) results in the elliptic modified Helmholtz problem

$$D\Delta\hat{u} - s\hat{u} = -u_0(z), \qquad z \in \mathbb{C} \setminus \Omega; \tag{5a}$$

$$\hat{u} = f(z)/s, \qquad z \in \partial\Omega. \tag{5b}$$

The next step in our approach is to seek a particular solution so that the governing equation (5a) becomes homogeneous at the expense of perturbing the boundary conditions. First, we introduce the free space Green's function $G(z,\xi;s)$ satisfying

$$D\Delta G - sG = \delta(z-\xi), \qquad z \in \mathbb{C} \setminus \{\xi\}; \tag{6a}$$

$$G(z,\xi;s) = \frac{1}{2\pi D}K_0(\alpha|z-\xi|), \qquad \alpha = \sqrt{\frac{s}{D}}. \tag{6b}$$

where $K_0(z)$ is the modified Bessel function of the second kind. In terms of the Green's function (6), we can decompose the solution of (5) into a particular solution $\hat{u}_p$ and homogeneous solution $\hat{u}_h$. Specifically, we have that

$$\hat{u}(z;s) = \hat{u}_p(z;s) + \hat{u}_h(z;s), \qquad \hat{u}_p(z;s) = \int_{\mathbb{C}\setminus\Omega} G(z,\xi;s)u_0(\xi)d\xi. \tag{7}$$

The homogeneous equation $\hat{u}_h(z;s)$ satisfies

$$D\Delta\hat{u}_h - s\hat{u}_h = 0, \qquad z \in \mathbb{C} \setminus \Omega; \tag{8a}$$

$$\hat{u}_h = \tilde{f}(z;s), \qquad z \in \partial\Omega; \tag{8b}$$

where the boundary term is given by

$$\tilde{f}(z;s) = \frac{f(z)}{s} - \int_{\mathbb{C}\setminus\Omega} G(z,\xi;s)u_0(\xi)d\xi\,. \tag{8c}$$

In the next section, we describe a method for the solution of (8).

2.1 The Lightning Method.

To begin a description on our approach, we introduce the following family of functions

$$\phi_k(z,\xi;s) = \frac{1}{2\pi D}K_{|k|}(\alpha|z-\xi|)\frac{(z-\xi)^k}{|z-\xi|^k}, \qquad \alpha(s) = \sqrt{\frac{s}{D}}, \tag{9}$$

which are exact solutions of the homogeneous modified Helmholtz equation (8a) on $\mathbb{C} \setminus \xi$. Our method is to seek a solution to (8) in the form

$$\hat{u}_h(z;s) = \sum_{j=1}^{N_1}\left(a_j\phi_{-1}(z,z_j;s) + b_j\phi_1(z,z_j;s)\right) + \sum_{k=-N_2}^{N_2} c_k\phi_k(z,z_*;s) \tag{10}$$

where $a_j, b_j \in \mathbb{C}$ for $j = 1,\ldots,N_1$ and $c_k \in \mathbb{C}$ for $k = -N_2,\ldots,N_2$ are complex constants. It is important to remark that (10) is a general solution of the equation (8) and that the constants coefficients in the expansion must be chosen to enforce the boundary conditions.

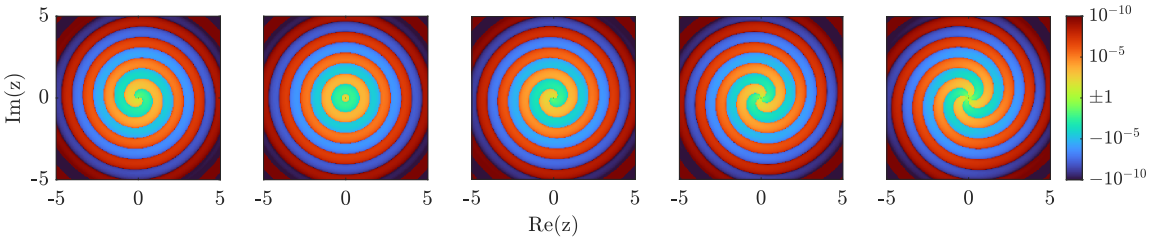

Fig. 2: Plots of $\mathrm{Re}\left(\phi_k\left(z,0;s\right)\right)$ and $k = \{-1,0,1,2,3\}$, $s = -15+30i$.

The first sum is referred to as the Newman part, and is analogous to the rational terms from the lightning Laplace approximations with poles $\{z_j\}_{j=1}^{N_1}$. The second sum is the Runge part, which can be understood as a higher order expansion about a single point z_*. The poles $\{z_j\}_{j=1}^{N_1}$ are chosen to resolve singularities such as those at the corners of our geometry. The role of the Runge part is to smooth out the solution on the rest of the boundary. A visualization of the first few modes $\mathrm{Re}(\phi_k)$ is shown in Fig. 2.

To describe the particular choice of N_1, N_2 for our algorithm, we first assign the N_B bodies with an overall total of N_v vertices/corners. We denote m to be the number of Newman poles per corner, implying $N_1 = mN_v$, and then set the order of each Runge expansion to be $N_2 = \mathcal{O}(\sqrt{m})$. Due to the complex coefficients in (10), our series has a total of $N = 2N_1 + 2N_2 + 1$ terms, and $2N$ degrees of freedom.

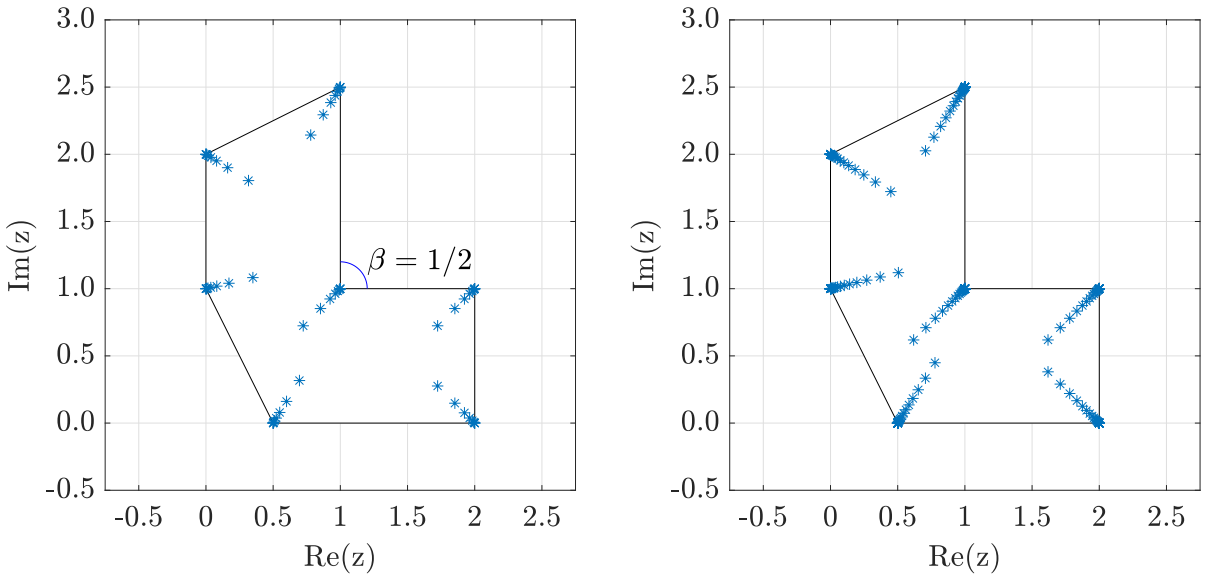

(a) 10 poles per corner.

(b) 50 poles per corner.

Fig. 3: Example of Newman pole clustering using the tapered distribution (12a), with σ in (12b).

2.2 Choice of Newman pole clustering.

In order to get accurate resolution of the solution and the corner singularities, one must carefully adapt the details of the clustering distributions of the Newman poles and the collocation points around them. Let us consider a corner at $z = 0$, and a distribution of points that are clustering towards it from the right (positive reals). A distribution first employed by [16] was of exponential form and given by

$$z_j = Ce^{-\sigma j/\sqrt{m}}, \qquad j = 0, \ldots, m-1. \tag{11}$$

The parameter σ controls the rate of clustering of points near the corner with empirical studies [16] suggesting the value $\sigma = 2.5$ generates a good balance between accuracy and computational effort.

A more recent analysis [20] suggested an improvement upon this, the so-called "tapered" distribution, given by

$$z_j = Ce^{-\sigma\left(\sqrt{m+1}-\sqrt{j}\right)}, \qquad j = 1, \ldots, m. \tag{12a}$$

Moreover, for the Laplace problem, the following choice of σ was proposed

$$\sigma = 2\sqrt{2-\beta}\pi, \tag{12b}$$

where $\beta \in (0, 2)$ is the exterior angle (modulo π) of the corner being clustered towards.

We implemented both of these clustering algorithms for the modified Helmholtz problem (8) and found the tapered to perform better overall and adopt this for the rest of the present work.

For a given geometry, we choose $C = \frac{\sqrt{2}}{2}h_{\min}$ where $h_{\min}$ is the minimum edge length of the entire geometry $\partial\Omega$. This choice guarantees that the poles remain in the interior of the geometry. For a corner in our geometry, we find the angular bisector and move this cluster of poles to be tangent with it. In Fig. 3 we show examples for $m = 10$ and $m = 50$ points per corner on a polygonal domain. We remark that due to floating point precision, some poles will round exactly to the vertex as m increases and lead to an ill-conditioned series. To ameliorate this, we remove any poles whose distance to the vertex lies within twice machine ε_M. These removal events also serve as a flag that increasing m further will not lead to improvements in accuracy.

2.3 Chebyshev collocation panels.

In order to form a linear system for the coefficients of the series (10), collocation points must cluster towards corners with at least the same rate as the Newman poles. The study of [15] used exponentially clustering of collocation points with a distribution $t \in [0, 1]$ between the midpoint and corner given by

$$f(t) = 1 - t^A e^{-\rho_c(1-t)}, \tag{13}$$

with parameter values $\rho_c = 4$ and varied A. An earlier version of the LM [17] used $A = 0$ and $\rho_c = -4\sqrt{m}$. While the details of the parameters may vary, the broad idea is to create a balance of points towards the corner and midpoint of each edge such that the distribution near the corner matches that of the Newman pole distribution while not under-resolving the center.

In our work, we have implemented a method where a single panel of Chebyshev nodes is replicated recursively on a sequence of sub-intervals, halving the distance to the corner with each iteration. Our method seeks to automatically determine the number of subdivisions (n_k) and Chebyshev points per panel (n_p) for a given number of collocation points N_c. First, we pick n_k large enough so that one panel is contained completely inside the ball between a corner and its closest Newman pole. Following this, we choose n_p so that the target number N_c is reached. We find this to robustly resolve both the corners and midpoints, while sacrificing speed by usually requiring a larger multiple of collocation points (which, as we are solving least squares for a series of fixed length, only scales linearly with time.) Hence for improved resolution of corners, we can increase the number of subdivisions n_k, while the resolution in the middle of edges can be tuned with the number of Chebyshev points per panel n_p. Two examples of our collocation panels are shown in Fig. 4.

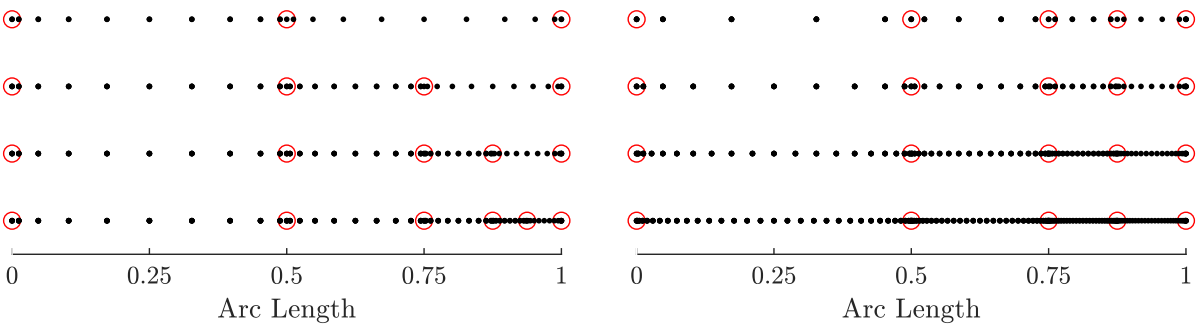

(a) Fixed n_p for varied $n_k = 1, \ldots, 4$.

(b) Fixed $n_k = 3$ for varied $n_p = 5, 10, 16, 32$.

Fig. 4: Examples of collocation grids from the midpoint ($t = 0$) to the corner ($t = 1$). Each grid has n_k subdivisions and n_p Chebyshev points per panel.

2.4 Numerical inversion of the Laplace transform.

In this section we describe our process for inverting the Laplace transform to return to time space. The inverse Laplace transform is defined by the Bromwich integral, given by

$$u(z;t) = \mathcal{L}^{-1}(\hat{u}) = \frac{1}{2\pi i}\int_B \hat{u}(z;s)e^{st}ds, \tag{14}$$

where $B = \{\gamma + is | s \in \mathbb{R}\}$ is the Bromwich contour. The value $\gamma \in \mathbb{R}$ is selected so that all poles of $\hat{u}(z;s)$ with respect to s are to the left of $\mathrm{Re}(s) = \gamma$. The integrand of (14) tends to be oscillatory along B which can

require a lot of terms to compute. However, since our problem has poles that lie solely along the negative real axis, we can deform the contour of integration into the left hand plane so that the integrand of (14) decays rapidly. The optimal choice of contour should balance moving into the left half-plane rapidly while not getting too close to the singularities, nor too far such that the exponential factor in (14) becomes very large. A highly optimized choice, known as the modified Talbot contour [12], is given by the general form

$$B_T = \Big\{ \frac{2M}{t}\rho(\theta) \,|\, -\pi < \theta < \pi \Big\}, \qquad \rho(\theta) = \big(-\sigma + \mu\theta\cot(\alpha\theta) + \nu i\theta \big), \tag{15a}$$

where $2M$ is the number of quadrature points applied to approximate the integral (see Fig. 5). A saddle point analysis [12] yields the following values which optimize the convergence rate:

$$\sigma = 0.6122, \qquad \mu = 0.5017, \qquad \alpha = 0.6407, \qquad \nu = 0.2645. \tag{15b}$$

The parametrization of B_T given in (15), expresses the integral as

$$u(z;t) = \frac{M}{\pi i t}\int_{-\pi}^{\pi} \hat{u}\Big(z; \frac{2M\rho(\theta)}{t}\Big) e^{2M\rho(\theta)}\rho'(\theta)d\theta = \mathrm{Re}\left[\frac{2M}{\pi i t}\int_{0}^{\pi} \hat{u}\Big(z; \frac{2M\rho(\theta)}{t}\Big) e^{2M\rho(\theta)}\rho'(\theta)d\theta\right]. \tag{16}$$

In the second step of (16), the symmetry of (15) has been used to express the integral as twice the real part of the value along the upper branch. The contour (15) is particularly effective for the present case of parabolic problems whose singularities lie along the negative real axis. The theoretical convergence rate is $\mathcal{O}(10^{-1.2M})$. Our validation of this convergence rate is presented in Fig. 7.

Given a fixed M, our approximation method is as follows: Discretize $(0,\pi)$ at equally spaced points $\theta_1, \ldots, \theta_M$ with step-size $h = \pi/M$. For a given $t > 0$, define $\omega(\theta) = e^{2M\rho(\theta)}\rho'(\theta)$ and $s(\theta) = 2M\rho(\theta)/t$. We then evaluate weights $\omega_j = \omega(\theta_j)$ and points $s_j = s(\theta_j)$ to define the midpoint quadrature rule

$$u(z;t) = \mathrm{Re}\Big(\frac{2}{it}\sum_{j=1}^{M}\omega_j\hat{u}(z;s_j)\Big), \qquad \theta_j = \Big(j - \frac{1}{2}\Big)\frac{\pi}{M}, \qquad j = 1, \ldots, M. \tag{17}$$

We remark that this choice of contour has the advantage of converging very rapidly and with errors reduced to near machine precision using $M = 9$ transform evaluations. Additionally, as the numerical examples of Sec. 4 will demonstrate, this integration method is robust over a wide range of times $t \in (0, \infty)$. A disadvantage of this approach is that it incurs a significant computational cost to recompute the transforms $\hat{u}(z; s_j)$ for each specified value of t. In the conclusion, we discuss methods for ameliorating this burden.

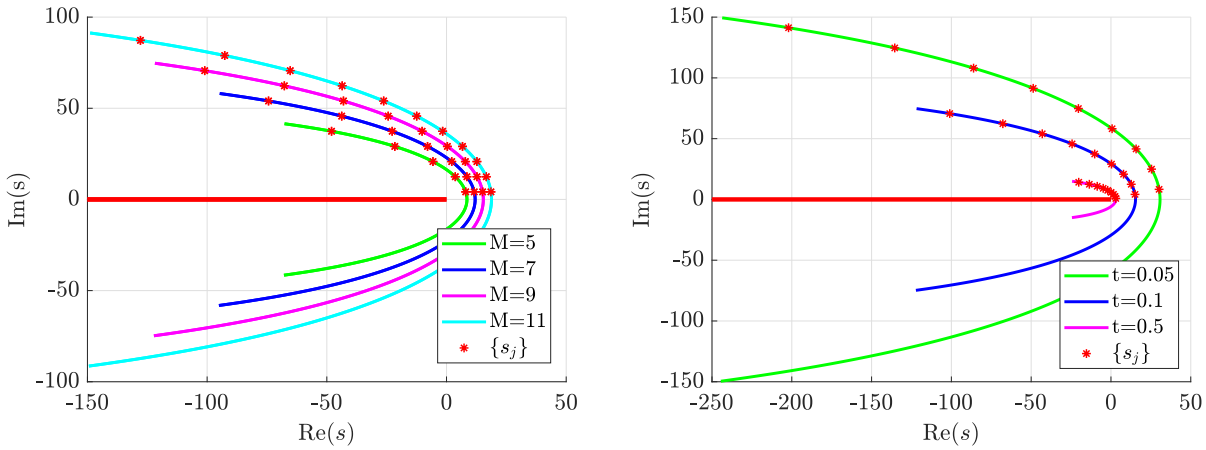

(a) Talbot contours for $t = 0.1$ and varied M.

(b) Talbot contours for $M = 9$ and varied t.

Fig. 5: The Talbot contour (15) and the mid-point quadrature points $\{s_j\}$. Shown are contours and their discretizations for fixed $t = 0.1$ and varying M (left) and varying t with fixed $M = 9$ (right).

3 Comparable methods for numerical validation.

We need various ways to validate and benchmark our solution. On most domains, analytical solutions of the PDE are difficult, and hence we will validate with other numerical and asymptotic methods. One particular approach will be to validate with Kinetic Monte Carlo (KMC) and asymptotic methods for representing the flux into absorbing targets [9]. The surface flux $j(t) = \int_{\partial\Omega} D\partial_n u ds$ of our approximation will be calculated by numerically integrating the analytical form of the normal derivative. This allows the cumulative fluxes $c(t)$, defined in (2), to be calculated and compared across the three methods.

3.1 Kinetic Monte Carlo (KMC) methods

In the particular case of solving (1) when $f \equiv 0$ and the initial condition is given by a Dirac source, $u_0(z) = \delta(z - z_0)$, we corroborate with a complementary method for solving the PDE (1) through sampling of the Langevin equation (3). The KMC method is a technique that massively accelerates the sampling of (3) by breaking down random paths into simpler geometric steps, or projectors, that can be solved exactly and tabulated for rapid access. By carefully combining several projection steps, it is possible to create exact simulations in arbitrary geometries in two and three dimensions [22,9,34,4,51]. The simulation of the paths (3a), and the statistics of arrivals of particles to $\partial\Omega$, gives Monte-Carlo estimates for the quantities (3b) which we can compute from our LM solution of (1). This provides a highly non-trivial method for validating our results over wide timescales.

3.2 Matched asymptotic expansion solution for multiple bodies.

The method can trivially be extended to multiple bodies by adding collocation points together with corresponding Newman and Runge expansions to the series approximation. This allows us to approximate the solution of (1) around multiple bodies. A useful validation of this approximation will be a recent matched asymptotic solution of (1), derived in the limit of small well-separated bodies [9]. We now give a brief statement of this result.

Consider N_B bodies $\{\Omega_k\}_{k=1}^{N_B}$ centered at positions $\{z_k\}_{k=1}^{N_B}$ with a common scale factor ε. The explicit form of each body is

$$\Omega_k = z_k + \varepsilon\,\mathcal{A}_k, \qquad k = 1, \ldots, N_B,$$

where $\mathcal{A}_k$ describes the shape of the body. It was recently shown [9] that as $\varepsilon \to 0$, the solution of (5) is of form

$$\hat{u}(z;s) = G(z, z_0; s) - 2\pi D \sum_{k=1}^{N_B} S_k \nu_k G(z, z_k; s) + \mathcal{O}(\varepsilon), \qquad \nu_k = \frac{-1}{\log \varepsilon d_k}. \tag{18a}$$

Here G is the Green's function (6) and d_k is a constant called the *logarithmic capacitance* or *logarithmic capacity* [28,43,1] which is determined uniquely by the shape of $\mathcal{A}_k$ and described in more detail shortly. The *strengths* $\{S_k\}_{k=1}^{N_B}$ satisfy the linear system

$$(\mathcal{I} + 2\pi D\,\mathcal{G}\mathcal{V})\,\mathbf{S} = \mathbf{g}_0, \qquad [\mathcal{G}]_{i,j} = \begin{cases} R(s), & i = j, \\ G(z_i, z_j; s), & i \neq j. \end{cases} \qquad [\mathcal{V}]_{i,j} = \begin{cases} \nu_i & i = j, \\ 0, & i \neq j, \end{cases} \tag{18b}$$

where $\mathcal{I} \in \mathbb{R}^{N_B \times N_B}$ is the identity matrix, $\mathbf{S} \in \mathbb{R}^{N_B}$ and $\mathbf{g}_0 \in \mathbb{R}^{N_B}$ are given by

$$\mathbf{S} = [S_1, S_2, \ldots, S_{N_B}]^T, \qquad \mathbf{g}_0 = [G(z_1, z_0; s), G(z_2, z_0; s), \ldots, G(z_{N_B}, z_0; s)]^T. \tag{18c}$$

The matrix $\mathcal{G}$ describes the spatial interactions between the bodies while the vector $\mathbf{g}_0$ describes the influence of the initial location on each of the bodies. Here $R(s)$ is the regular part of $G(z,\xi;s)$ at the source. The small argument asymptotics $K_0(z) \sim -\log(z) + \log 2 - \gamma_e$ as $z \to 0$ give this term as

$$R(s) = \lim_{z\to\xi}\Big(G(z,\xi;s) + \frac{1}{2\pi D}\log|z-\xi|\Big) = \frac{1}{2\pi D}\Big(\log 2 - \gamma_e - \log\sqrt{s/D}\Big), \tag{19}$$

where $\gamma_e \approx 0.5772$ is the Euler-Mascheroni constant. The vector $\widehat{\mathcal{J}} = 2\pi D\mathcal{V}\mathbf{S}(s)$ describes the Laplace transform of the fluxes through each of the absorbers and is obtained from solving (18b). The logarithmic capacitance d_k is determined from the solution of the electrified disk problem

$$\Delta v_k = 0; \quad \text{in} \quad \mathbb{C}\setminus\mathcal{A}_k; \qquad v_k = 0, \quad \text{on} \quad \partial\mathcal{A}_k; \tag{20a}$$

$$v_k = \log|z| - \log d_k + \mathcal{O}(|z|^{-1}), \qquad |z|\to\infty. \tag{20b}$$

For a variety of regular shapes, the value of d_k is known explicitly. Some examples include (see also [28])

$$d_k = \frac{\Gamma(\frac{1}{2})}{4\pi^{\frac{3}{2}}}h \approx 0.590h \qquad \text{Square of side-length } h. \tag{21a}$$

$$d_k = \frac{\sqrt{3}\Gamma(\frac{1}{3})^3}{8\pi^2}h \approx 0.422h \qquad \text{Equilateral triangle of side-length } h. \tag{21b}$$

$$d_k = \frac{3^{\frac{3}{4}}\Gamma(\frac{1}{4})^2}{2^{\frac{7}{2}}\pi^{\frac{3}{2}}}h \approx 0.476h \qquad \text{Isosceles right triangle with small side-length } h. \tag{21c}$$

When the shape of the body is completely general, there are several numerical algorithms that can approximate the capacitance [31, 1]. Hence, given the centering coordinates of the absorbers and their capacitance values d_k, we solve the linear system (18b) and form the flux vector $\widehat{\mathcal{J}} = 2\pi D\mathcal{V}\mathbf{S}(s)$ which is inverted using the Talbot method described in Sec. 2.4. This yields the time-dependent fluxes $j_k(t) = \int_{\partial\Omega_k} D\partial_n u\, ds$ and cumulative fluxes $c_k(t) = \int_0^t j_k(\tau)d\tau$ into each individual absorber which will be compared to corresponding quantities obtained from the LM and KMC solutions.

4 Numerical Results.

In this section, we provide a variety of examples that validate our method for single and multiple bodies. Initially, we will show the effect of varying the number of transform evaluations M in the inverse Laplace transform procedure, eventually adopting $M = 9$ as the default parameter. In each of the examples shown, the diffusivity takes the value $D = 1$. We will examine the accuracy of the method by determining the errors

$$\mathcal{E}^\infty[\hat{u}] = \sup_{z\in\partial\Omega}\|\hat{u}(z;s) - f(z)/s\| \tag{22a}$$

$$\mathcal{E}^\infty[u] = \sup_{z\in\partial\Omega}\|u(z,t) - f(z)\| \tag{22b}$$

Recall that $\hat{u} - f(z)/s = \hat{u}_h + \hat{u}_p - f(z)/s = \hat{u}_h - (f(z)/s - \hat{u}_p) = \hat{u} - \tilde{f}$, so the error is equivalent to the error between $\hat{u}_h$ and $\tilde{f}$ from (8c). Accordingly, when taking relative error, we scale by the factor $\sup_{z\in\partial\Omega}\|\tilde{f}(z;s)\|$ in the Helmholtz problem, and the equivalent in the heat problem. We approximate these errors by oversampling on $\partial\Omega$ with distribution (13) with $A = 0$, $\rho_c = 60$, so that we interpolate densely between the Chebyshev panels.

Unless stated otherwise, our primary demonstrations will set $f(z) \equiv 0$, and $u_0(z) = \delta(z - z_0)$ for some z_0, solving the underlying problem for calculating FPT distributions (2). Recalling that our number of degrees of freedom is $2N$, we form our overdetermined linear system by setting the number of collocation points at $N_c = 7\times 2N$. Finally, we choose $N_2 = 4\sqrt{m}$ as the order of our Runge expansions.

4.1 Example: Convergence analysis of Talbot integration for a single square absorber.

In this example, we perform validations and examine the convergence properties of the inverse Laplace transform method. Specifically, we seek to demonstrate the appropriate number M of transform evaluations to apply in the Talbot quadrature equation (16). In Fig. 6, we display solutions $u(z,t)$ of the system (1) for the scenario where Ω is a single square absorber with vertices $\pm 1 \pm i$ and the initial data is specified as $u_0(z) = \delta(z-2)$. We fix our solution with $m = 90$ Newman poles per corner to attempt so that the errors in modified Helmholtz solution are dominated by the Talbot quadrature. When plotted on a logarithmic scale, the solutions reveal (cf. Fig. 6(a,b)) exponentially small spurious oscillations when $M = 3, 6$ which are resolved (cf. Fig. 6(c,d)) for $M = 9, 12$.

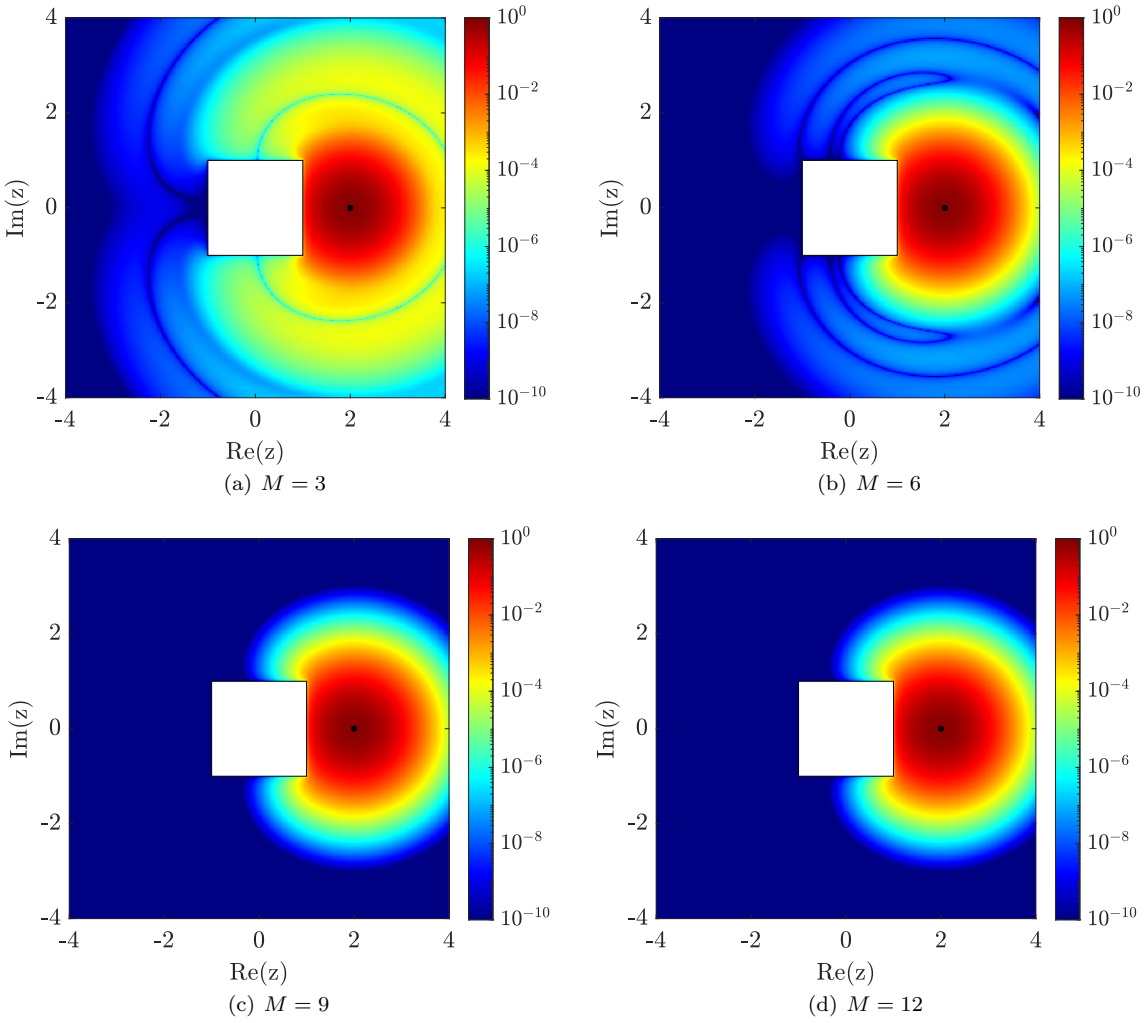

(a) $M = 3$ (b) $M = 6$

(c) $M = 9$ (d) $M = 12$

Fig. 6: Solution $|u(z,t)|$ of (1) at $t = 0.1$ with various number M of Laplace transform evaluations. Increasing M removes spurious oscillations in the solution.

In Fig. 7, we approximate the L_∞ error by finely sampling our solution in the bulk, and taking the maximum error between our solution for a given M and our solution for $M = 15$. We observe the relative error decreasing as a function of transform evaluations M, in agreement with the theoretical convergence rate [12]. The choice of $M = 9$ is observed to push the error in the bulk close to 10^{-10}, which we will adopt as our target accuracy for our other numerical demonstrations.

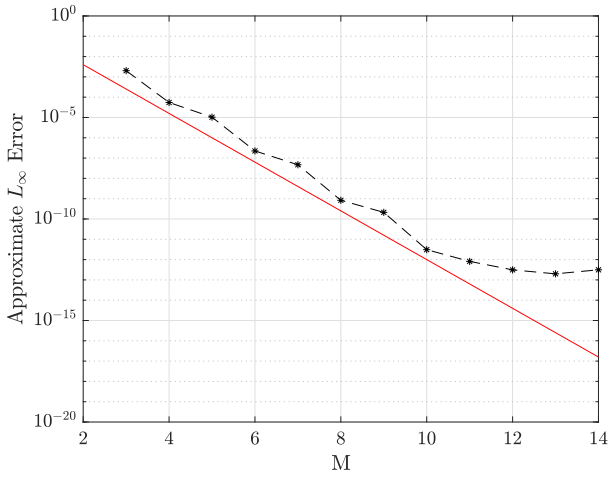

Fig. 7: Convergence of the Talbot method with respect to the number M of transform evaluations. The approximate L_∞ error against M agrees with the theoretical convergence rate $\mathcal{O}(10^{-1.2M})$ (straight red line).

With a sufficient M chosen for our target accuracy, we conduct additional convergence studies for the LM method. First, using the same square configuration with a point source at $z_0 = 2$, we calculate the $\mathcal{E}^\infty$ error as defined in (22a) and (22b) for an increasing number of terms N. We solve (1) at $t = 0.1$, as in the previous figure, and for appropriate comparison we solve (5) for various s values present in the associated Talbot contour for $t = 0.1$. In Fig. 8, we observe the convergence rate to be linear against $\sqrt{N}$, validating the root-exponential convergence of the LM. We see our method is capable of attaining a relative error around 10^{-10} across a range of s-values. This bound on the error is consistent with those observed in the LM literature and is due to the process of solving with an overdetermined basis [16].

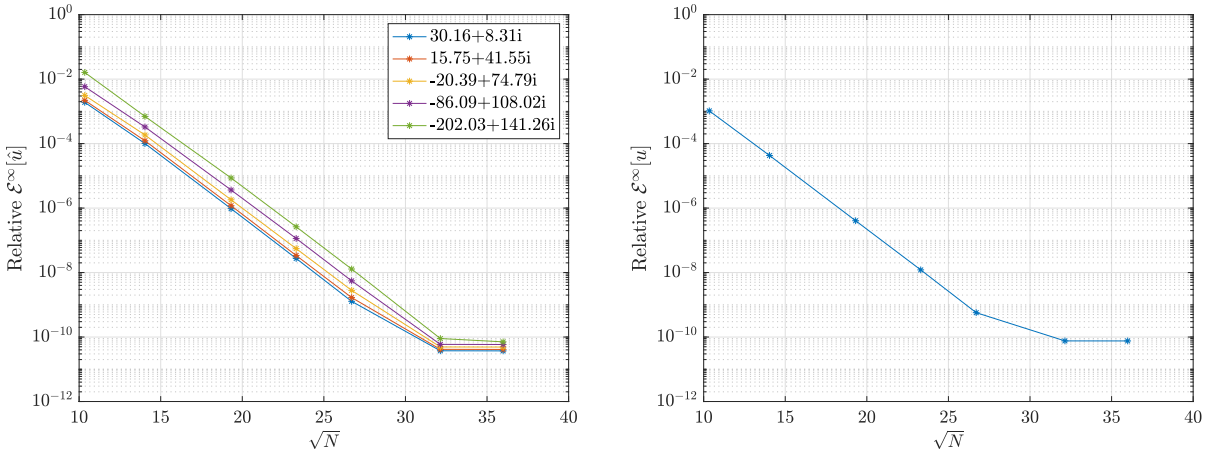

(a) Convergence of errors for $\hat{u}(z, s)$.

(b) Convergence of errors for $u(z, t)$.

Fig. 8: Convergence of the relative errors in the Laplace and time domains for the case of a single square absorber. Panel (a): Convergence studies for approximation with square root of increasing terms $\sqrt{N}$ of (5) for various s in the contour for $t = 0.1$. Panel (d): Convergence of error in approximation of solution of equation (1) at $t = 0.1$.

In Fig. 9, we plot solutions of (5) for several values of s corresponding to the Talbot contour of $t = 0.1$. Also shown is the relative residual, and the relative error on the same over-sampled grid that $\mathcal{E}^\infty[\hat{u}]$ is calculated to demonstrate the method acquiring an appropriate measurement of the error along the boundary.

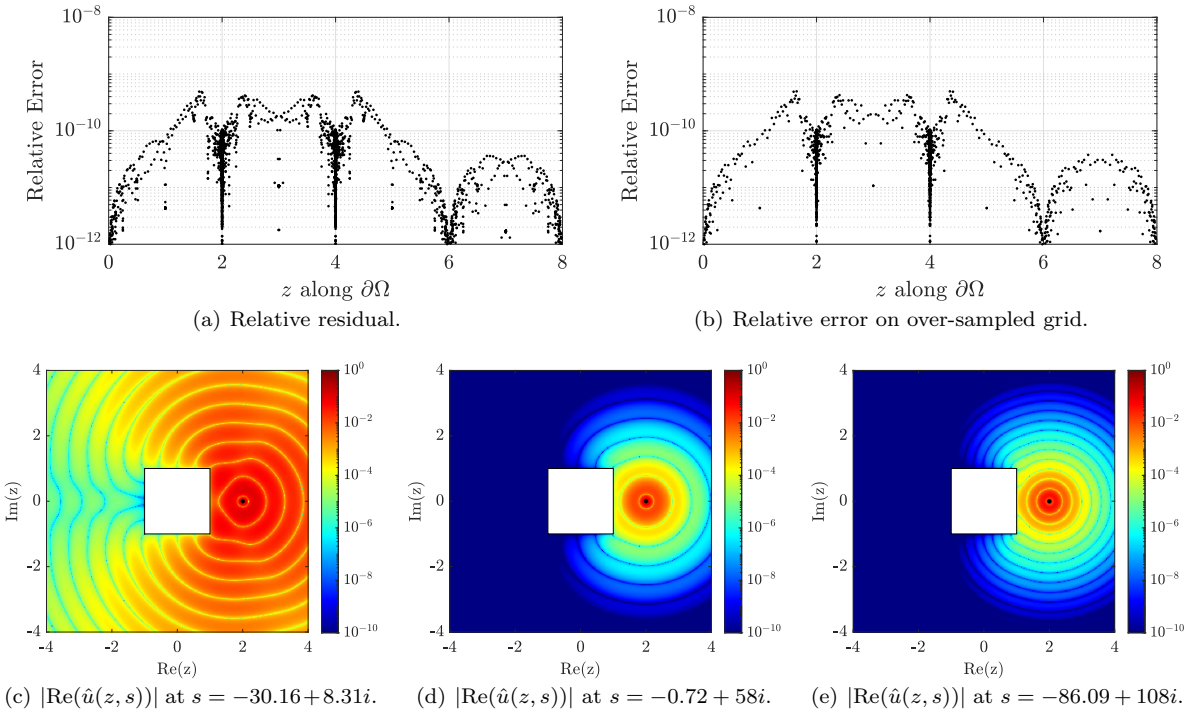

(a) Relative residual.

(b) Relative error on over-sampled grid.

(c) $|\mathrm{Re}(\hat{u}(z,s))|$ at $s = -30.16 + 8.31i$.

(d) $|\mathrm{Re}(\hat{u}(z,s))|$ at $s = -0.72 + 58i$.

(e) $|\mathrm{Re}(\hat{u}(z,s))|$ at $s = -86.09 + 108i$.

Fig. 9: Panels (a-b): Point-wise residual and over-sampled relative error (22a) of solution to (5) on the boundary $\partial\Omega$ for $s = -20 + 74i$, with $m = 80$. Panels (c-e): Approximate solution of (5) for various s in the Talbot contour of $t = 0.1$, with $m = 80$. $\mathcal{E}^{\infty}[\hat{u}]$ for each given by (c) 7.82×10^{-10}, (d) 3.08×10^{-10}, (e) 1.38×10^{-9}.

4.2 Example: Simulation for a single triangular absorber.

In this example, we consider a single triangular absorber centered at $z = 0.5{+}0.5i$ with vertices $\{1{+}0.5i, i, 0\}$. The centering point z_* of the Runge expansion is the centroid of the triangle. The solution $u(z,t)$ of (1) is calculated for $f \equiv 0$ and $u_0(z) = \delta(z - z_0)$ where $z_0 = 2.5 + 0.5i$. In Fig. 10 we plot solutions at 6 time points showing shortly after initialization, and the engagement with the body. In particular, we remark that the method captures the "shadow" region in the rear of the body where the solution has lower value. Probabilistically, the lower values reflects the observation that a diffusing particle is much less likely to be present at this location.

4.3 Example: Comparison of lightning method with KMC and matched asymptotic expansions.

In this example we compare the solution of (1) from the LM with two recently developed alternative methods, a particle based Kinetic Monte Carlo (KMC) method and a matched asymptotic expansion. The asymptotic approximation, as summarized in Sec. 3.2, is derived in the limit of well separated bodies [9]. In our experiments, we calculate and compare the cumulative density functions $c(t)$, defined in (2), with each of these methods.

Our first configuration consists of a point source at $z_0 = 0$ diffusing to $N_B = 3$ bodies; an equilateral triangle centered at $z_1 - 1 + 2.5i$, a square centered at $z_2 = -2 - i$, and an isosceles triangle with centroid at $z_3 = 3 - 3i$. The side lengths of the square and triangle, and the small-side length of the isosceles triangle are uniformly $h = 0.3$. The flux vector is calculated from the asymptotic formula (18) and then inverted with $M = 9$ points. The KMC simulation is run with 1×10^6 particles. In Fig. 11, we plot the solution $u(z,t)$ at $t = 1$ and highlight again the shadow effect where the occupation probability behind the target

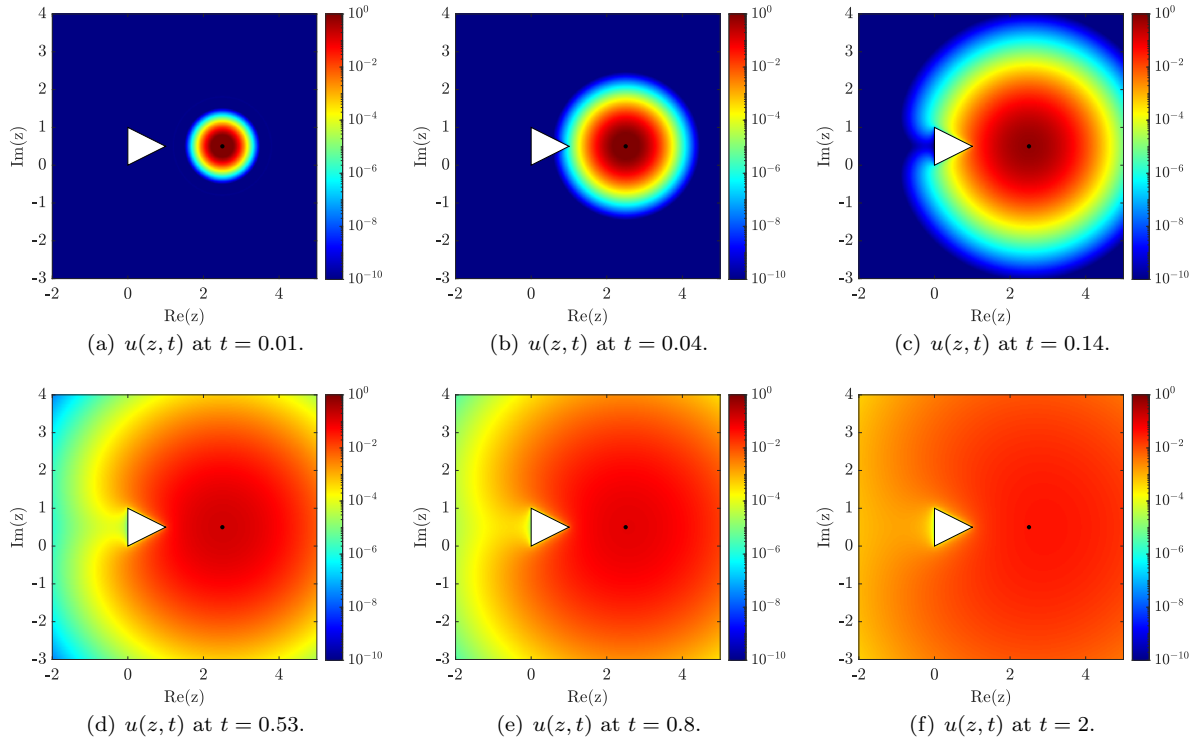

(a) $u(z,t)$ at $t = 0.01$. (b) $u(z,t)$ at $t = 0.04$. (c) $u(z,t)$ at $t = 0.14$.

(d) $u(z,t)$ at $t = 0.53$. (e) $u(z,t)$ at $t = 0.8$. (f) $u(z,t)$ at $t = 2$.

Fig. 10: LM solution $u(z,t)$ of (1) for the case of a single triangular absorbing body with initial condition $u_0(z) = \delta(z - (2.5 + 0.5i))$, $m = 120$. Solutions shown a sequence of times from $t = 0.01$ to $t = 2$.

is markedly lower. The agreement between the cumulative fluxes $c(t)$ from the LM, KMC and asymptotic methods is very good (cf. Fig. 11(d)).

For our next configuration, we consider $N_B = 8$ bodies of various h and rotations in an integer grid with spacing 2 and a point source at $z_0 = -2$. Rotations are sampled uniformly on $[0, 2\pi)$ and side lengths are normally distributed with mean 0.3 and standard deviation 0.2 with positivity enforced. The domain and three solutions $u(z,t)$ of (1) are shown in Figs. 12(a-c). Solutions are also calculated from the matched asymptotic expansion and the KMC method. We choose half of the bodies to be equilateral triangles, and half to be squares, and calculate their combined fluxes, once again attaining very close agreement (cf. Fig. 12(d)). Given the fact that these three solutions are generated by completely different methods, their remarkably good agreement serves as a highly non-trivial validation of the LM approach.

4.4 Example: Nonzero boundary conditions.

Our previous examples focused on the homogeneous boundary condition $u(z,t) = f(z) \equiv 0$ on $\partial\Omega$ and the initial condition $u(z,0) = \delta(z - z_0)$. In this section, we demonstrate the application of the LM method to nonzero boundary conditions. We impose the condition $f(z) = \mathrm{Re}(z)^{10}$ In Fig. 13 we plot the solution $u(z,t)$ of (1) at several time points for the initial condition $u_0(z) = \delta(z - z_0)$ and $z_0 = 1.5$.

4.5 Example: L-shaped domain and multiple Runge poles.

As remarked in other works [16], elongated domains pose a difficulty to lightning solvers due to the Runge expansion decaying as it approaches $\partial\Omega$ and becoming an ill-conditioned basis. As $K_n(z)$ decays exponentially as $z \to \infty$, as opposed the polynomial rate associated to rational functions or other Bessel functions, we observe a slower rate of convergence in certain examples.

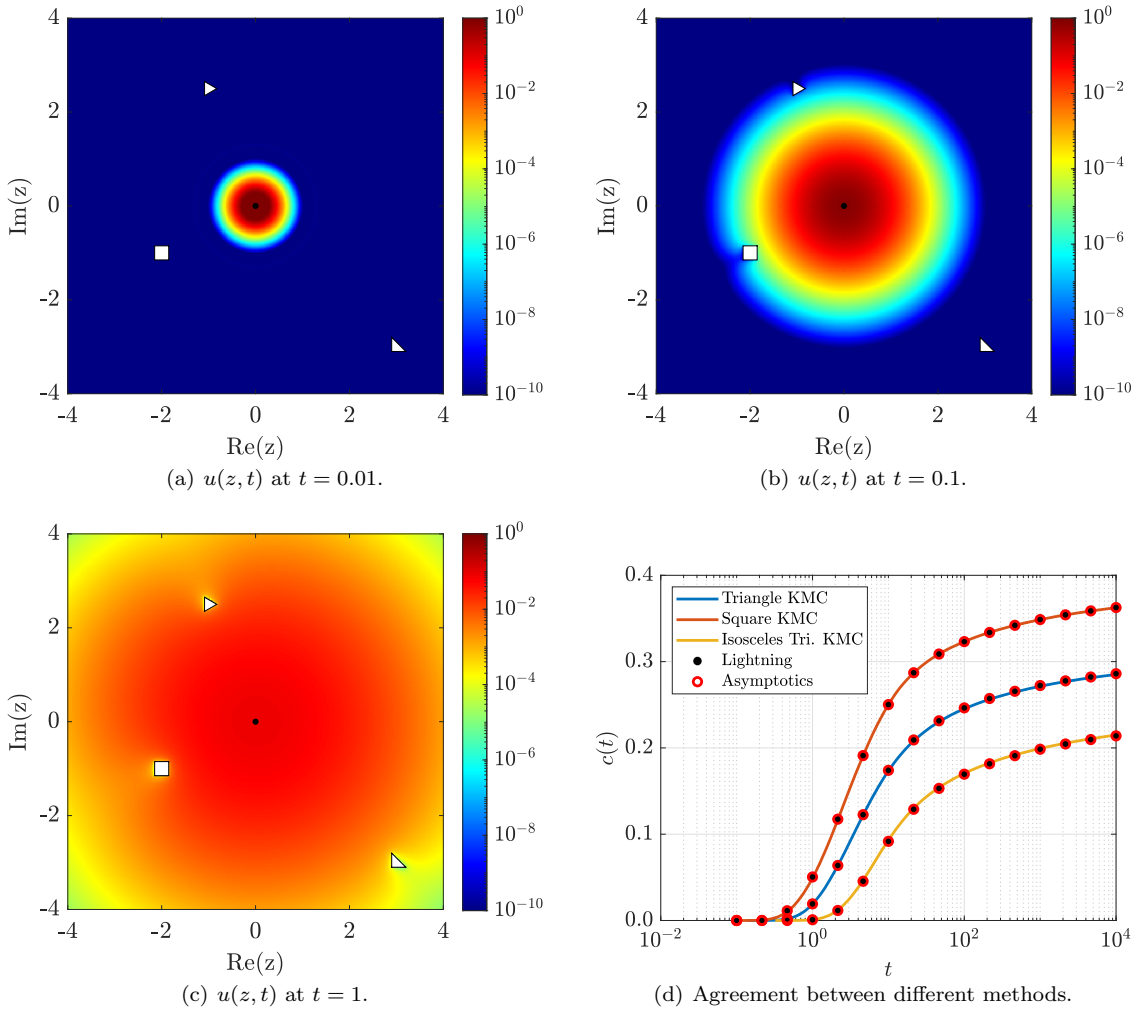

(a) $u(z,t)$ at $t = 0.01$. (b) $u(z,t)$ at $t = 0.1$.

(c) $u(z,t)$ at $t = 1$. (d) Agreement between different methods.

Fig. 11: Panels (a-c): Solutions $u(z,t)$ of (1) with three small absorbers with $u_0(z) = \delta(z)$ and $m = 80$ at various t from 0.01 to 1. Panel (d): Agreement of the capture rate (2) at individual absorbers as computed from the LM, the asymptotic solution (18) and the KMC method [9].

We demonstrate this phenomenon in the convergence rate for the case of the L-shaped domain with a single Runge pole at $z_* = 0.8{+}0.8i$ (cf. Fig. 14). We solve this problem at various times and for configurations of source locations, close and far from the re-entrant corner. We observe in each case, the root exponential convergence is maintained, albeit at a much slower rate and we do not reach our target error 10^{-10}, as shown in Fig. 14(d).

As a demonstration of a potential resolution of this issue, we show that placing multiple Runge expansions into our series representation of the solution yields an improved rate of convergence and reduction in error. In Fig. 15, we show results for two Runge expansions centered at the points $z_{*1} = 1 + 0.5i$ and $z_{*2} = 0.5 + i$. As seen in the solution profiles $u(z,t)$ in Figs. 15(a-c), the solution is now well resolved near the boundary. Indeed, in Fig. 15(d), we see a dramatic improvement in the convergence rate of the method.

4.6 Example: Solution for general initial conditions.

For the choice of a point source initial condition $u_0(z) = \delta(z - z_0)$, the boundary term (8c) reduces to

$$\tilde{f}(z;s) = \frac{f(z)}{s} - \int_{\mathbb{C}\setminus\Omega} u_0(z) G(z,\xi;s) d\xi = \frac{f(z)}{s} - G(z,z_0;s).$$

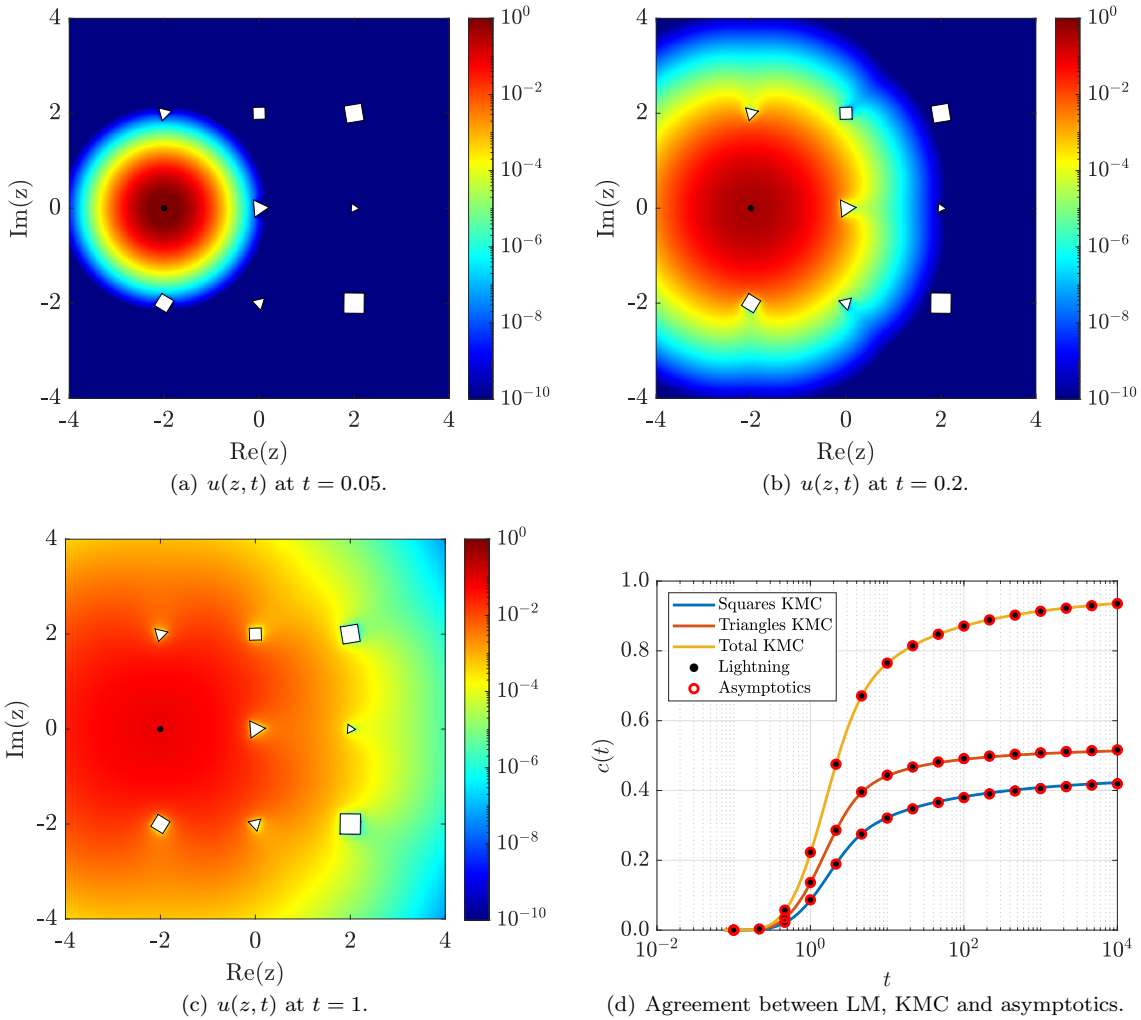

(a) $u(z,t)$ at $t = 0.05$.

(b) $u(z,t)$ at $t = 0.2$.

(c) $u(z,t)$ at $t = 1$.

(d) Agreement between LM, KMC and asymptotics.

Fig. 12: Panels (a-c): LM solution $u(z,t)$ of (1) with $m = 80$. Panel (d): Cumulative fluxes $c(t)$ through all squares, all triangles, and all bodies computed by LM, KMC and matched asymptotic expansions.

which is readily evaluated. In this example, we demonstrate the applicability of the method for the more general initial condition $u_0(z) \in [0,1]$ shown in (cf. Fig. 16). This function is compactly supported on $\mathbb{R}^2$ and we evaluate the integral term $\hat{u}_p$ in (7) via quadrature. The shown solution profiles $u(z,t)$ display the smoothing effects of the heat equation on the discontinuities in the initial profile. For our geometry, we adopt our configuration in Fig. 3 with Runge expansions at $z_{*1} = 5 + 2.5i$ and $z_{*2} = 4.5 + 3i$.

5 Discussion.

In this work we have developed a lightning solver for the heat equation in unbounded planar regions with disjoint absorbing bodies. Our approach provides a complement to recent adaptations of the lightning method to Laplace, Helmholtz and Stokes problems and further highlights its usefulness in the numerical computation of solutions to an important class of challenging problems where geometric corners induce solution singularities. Our method has been validated on several complex examples and through comparison with solutions via complementary techniques such as Monte Carlo methods and matched asymptotic expansions.

There are various avenues for future work that emanate from this study. Our applications have focused solely on the case of Dirichlet absorbers, however, it is natural to consider additional boundary conditions, such as Neumann and Robin which appear in numerous biological signaling problems. In rudimentary

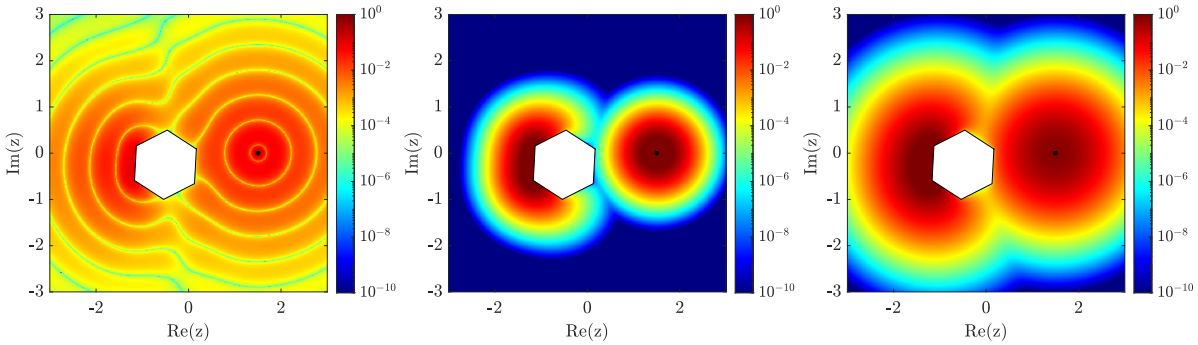

(a) $|\mathrm{Re}(\hat{u}(z,s))|$ at $s=-30-21i$. (b) $u(z,t)$ at $t=0.03$. (c) $u(z,t)$ at $t=0.1$.

Fig. 13: The LM method for the solution of (1) with a single hexagonal body, the applied boundary condition $u=f(z)=\mathrm{Re}(z)^{10}$ on $\partial\Omega$ and the initial condition $u_0=\delta(z-z_0)$ for $z_0=1.5$ and $m=90$. Panel (a): The solution of (5) at value $s=-30-21i$. Panel (b): The solution of the heat equation (1) at $t=0.03$. Panel (c) The solution $u(z,t)$ at $t=0.1$.

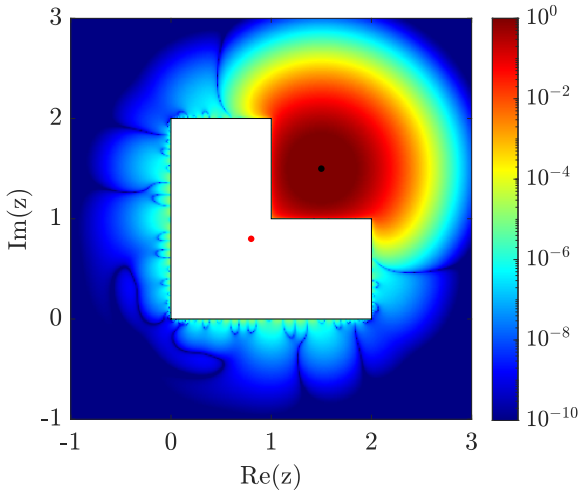

(a) $u(z,t)$ at $t=0.03$. Source at $z_0=1.5+1.5i$.

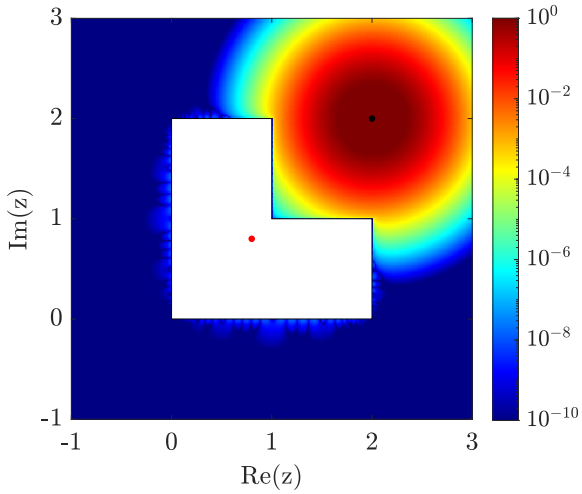

(b) $u(z,t)$ at $t=0.03$. Source at $z_0=2+2i$.

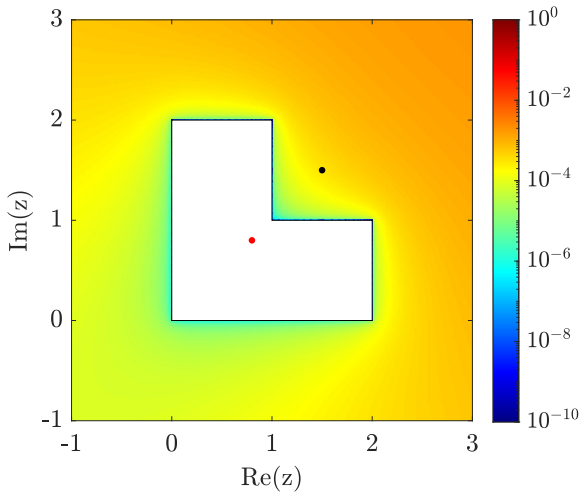

(c) $u(z,t)$ at $t=5$. Source at $z_0=1.5+1.5i$.

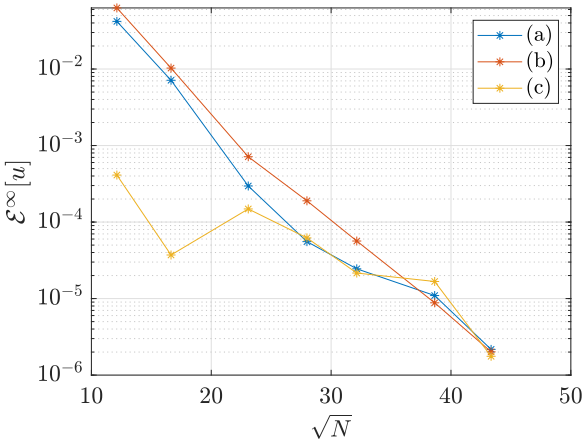

(d) Convergence of (a-c).

Fig. 14: Solutions of (1) for the L-shaped domain with $m=90$, $u_0=\delta(z-z_0)$ for various z_0 (solid black dot) and different times t. Calculations performed with a single Runge expansion centered at $z_*=0.8+0.8i$ (solid red dot). The resulting relative errors are (a) $\mathcal{E}^{\infty}[u]=5.1\times10^{-5}$, (b) $\mathcal{E}^{\infty}[u]=3.3\times10^{-5}$, (c) $\mathcal{E}^{\infty}[u]=1.03\times10^{-5}$. Panel (d): Convergence with respect to square root of number of terms for each configuration.

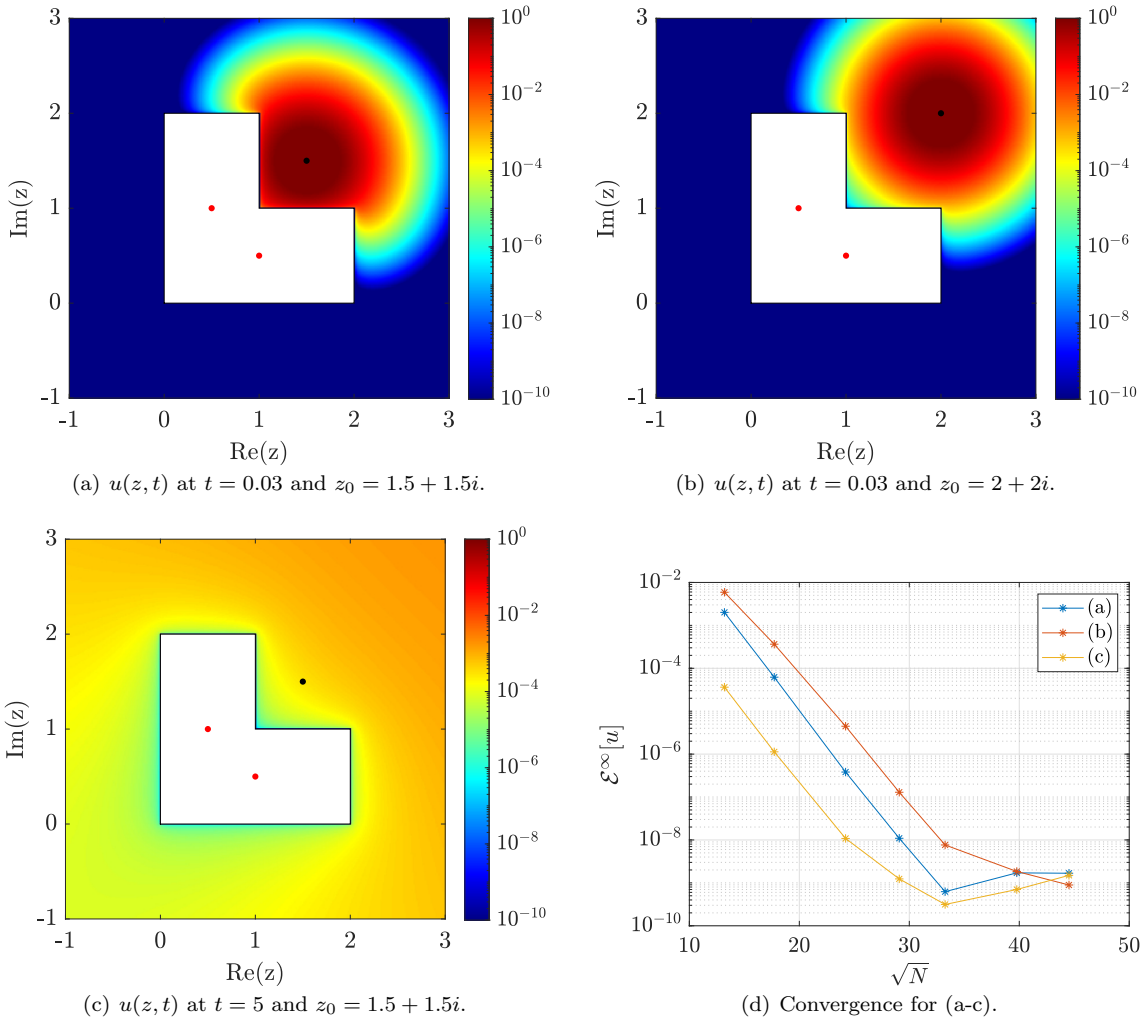

(a) $u(z,t)$ at $t = 0.03$ and $z_0 = 1.5 + 1.5i$.

(b) $u(z,t)$ at $t = 0.03$ and $z_0 = 2 + 2i$.

(c) $u(z,t)$ at $t = 5$ and $z_0 = 1.5 + 1.5i$.

(d) Convergence for (a-c).

Fig. 15: The L-shaped domain with two Runge expansions about points $z_{*1} = 1+0.5i$ and $z_{*2} = 0.5+i$ (solid red dots) with $m = 90$. The resulting relative errors are (a) $\mathcal{E}^{\infty}[u] = 4.0 \times 10^{-10}$, (b) $\mathcal{E}^{\infty}[u] = 2.14 \times 10^{-9}$ and (c) $\mathcal{E}^{\infty}[u] = 1.14 \times 10^{-10}$.

investigations on the applicability of this method to the case of all Neumann bodies, we observe that jump discontinuities of the normal derivative at corners can induce oscillations in the solution. A similar situation arises in the scenario of mixed boundary conditions in which a single absorber featuring a combination of Dirichlet and Neumann has singularities in the normal derivative at their meeting points, even along smooth boundaries. In certain scenarios, the singularity structure is known [3], hinting that recent methods for rational representation of functions z^{α} may be applicable to the solutions of these cases [20, 41].

There are several other aspects that may be adapted to improve the performance of the method presented here. One example is the log-lightning method which has been deployed for Laplace problems [48, 1] and improves the convergence rate from root-exponential to exponential. In another direction, we have noticed that the performance of the method can be drastically affected by the number and centering location(s) of the Runge expansion. In simple geometries, such as triangles or squares, a single Runge expansion located at the center of mass is very effective. However, in the example of the L-shaped domain (Fig. 15), we show that expanding around two Runge points dramatically improves performance.

While we discussed how the addition of more Runge expansions about separate centers can drastically improve convergence, we do not yet have an explicit way to assign them with respect to the geometry and where the Newman poles are located. For this, it seems profitable to explore computational geometry to determine algorithms for features that can help us robustly place them. The (topological) skeleton, or

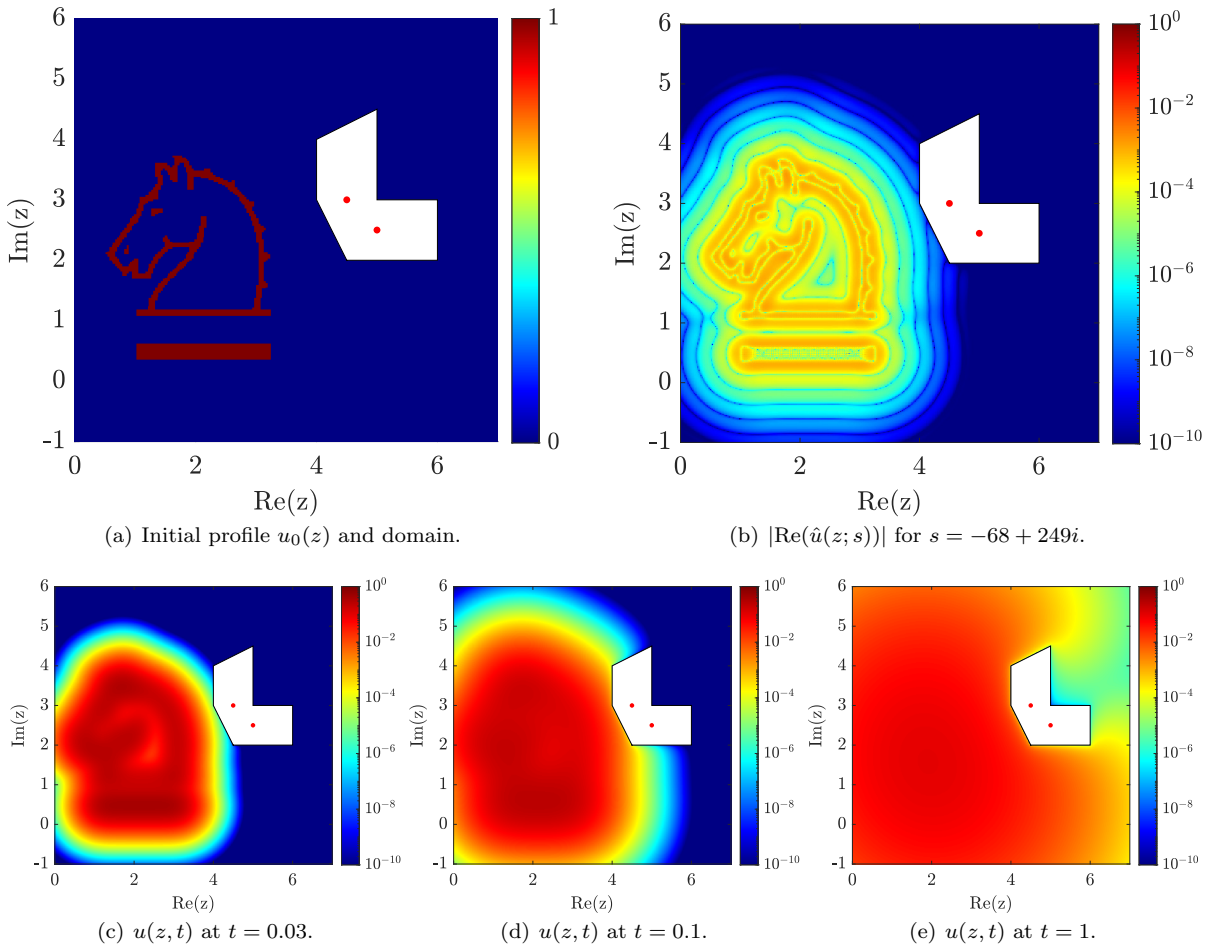

(a) Initial profile $u_0(z)$ and domain.

(b) $|\mathrm{Re}(\hat{u}(z;s))|$ for $s = -68 + 249i$.

(c) $u(z,t)$ at $t = 0.03$.

(d) $u(z,t)$ at $t = 0.1$.

(e) $u(z,t)$ at $t = 1$.

Fig. 16: The LM applied to equation (1) for $f = 0$, a single polygonal body and a general initial condition, all solved with $m = 90$. Panel (a): The domain and the initial profile $u_0(z)$ and two Runge poles (solid red dots). Panel (b): Solution of (5) for $s = -68 + 249i$. Panels (c-e): solutions $u(z,t)$ of (1) for various t.

medial axis of a planar graph/geometry is the set of all points that are equidistant to at least two points on the boundary [5]. Medial axes, and how to compute them are well studied, and contain information about the geometry that can be robustly recovered and used for applications [25], including predicting the location of singularities in non-linear PDEs [13,33,36]. One formulation of the skeleton contains a segment of each angular bisector, akin to where we place our Newman poles; suggesting one could similarly derive a consistently useful location for Runge poles. This approach could potentially further generalize the geometric regions that the LM method can be applied to.

Finally, we note that when the solution $u(z,t)$ of (1) is desired at many t values, there are certainly economies to be gained by reusing transform evaluations. The current Talbot contour (15) is robust across a wide range of values $t \in (0,\infty)$, but recomputes the coefficients $\{\hat{u}(z,s_j)\}_{j=1}^{M}$ at each time point. However, we have observed that other contour choices based on fixed coefficients, can be effective over large time ranges, thus hinting at the potential for an adaptive approach.

Acknowledgments

AEL acknowledges support from NSF grant DMS-2052636. The authors are grateful to Prof. Abinand Gopal for many useful discussions. HLC acknowledges support of the Arthur J. Schmitt Presidential Leadership fellowship.

Data availability statement

This work did not involve the use of data.

Declarations

The authors have no competing interests to declare that are relevant to the content of this article.

References

1. Baddoo, P., Trefethen, L.N.: Log-lightning computation of capacity and green's function. Maple Transactions **1**(1) (2021). DOI 10.5206/mt.v1i1.14124. URL https://mapletransactions.org/index.php/maple/article/view/14124
2. Baddoo, P.J.: Lightning solvers for potential flows. Fluids **5**(4) (2020). DOI 10.3390/fluids5040227. URL https://www.mdpi.com/2311-5521/5/4/227
3. Bernoff, A.J., Lindsay, A.E.: Numerical approximation of diffusive capture rates by planar and spherical surfaces with absorbing pores. SIAM Journal on Applied Mathematics **78**(1), 266–290 (2018)
4. Bernoff, A.J., Lindsay, A.E., Schmidt, D.D.: Boundary homogenization and capture time distributions of semipermeable membranes with periodic patterns of reactive sites. SIAM Journal on Multiscale Modeling & Simulation **16**(3), 1411–1447 (2018)
5. Blum, H.: A transformation for extracting new descriptions of shape. Models for the perception of speech and visual form pp. 362–380 (1967)
6. Bressloff, P.C., Newby, J.M.: Stochastic models of intracellular transport. Reviews of Modern Physics **85**, 135–196 (2013). DOI 10.1103/RevModPhys.85.135. URL https://link.aps.org/doi/10.1103/RevModPhys.85.135
7. Brubeck, P.D., Trefethen, L.N.: Lightning stokes solver. SIAM Journal on Scientific Computing **44**(3), A1205–A1226 (2022)
8. Chapko, R., Kress, R.: Rothe's Method for the Heat Equation and Boundary Integral Equations. Journal of Integral Equations and Applications **9**(1), 47–69 (1997)
9. Cherry, J., Lindsay, A.E., Hernández, A.N., Quaife, B.: Trapping of Planar Brownian Motion, Full First Passage Time Distributions by Kinetic Monte-Carlo, Asymptotic and Boundary Integral Equations. SIAM Journal on Multiscale Modelling and Simulation **20**(4), 1284–1314 (2022)
10. Cherry, J., Lindsay, A.E., Quaife, B.D.: Boundary integral methods for particle diffusion in complex geometries: Shielding, confinement, and escape. Journal of Computational Physics **534**, 114032 (2025). DOI https://doi.org/10.1016/j.jcp.2025.114032. URL https://www.sciencedirect.com/science/article/pii/S0021999125003158
11. Costabel, M., Sayas, F.J.: Time-dependent problems with the boundary integral equation method. Encyclopedia of Computational Mechanics **1**, 703–721 (2004)
12. Dingfelder, B., Weideman, J.A.C.: An improved talbot method for numerical laplace transform inversion. Numerical Algorithms **68**(1), 167–183 (2015)
13. DiPietro, K.L., Haynes, R.D., Huang, W., Lindsay, A.E., Yu, Y.: Moving mesh simulation of contact sets in two dimensional models of elastic–electrostatic deflection problems. Journal of Computational Physics **375**, 763–782 (2018). DOI https://doi.org/10.1016/j.jcp.2018.08.053. URL https://www.sciencedirect.com/science/article/pii/S0021999118305862
14. Fryklund, F., Kropinski, M.C.A., Tornberg, A.K.: An integral equation based numerical method for the forced heat equation on complex domains. Advances in Computational Mathematics **43**, 1–36 (2020)
15. Ginn, H.: Lightning helmholtz solvers. arXiv preprint (2022). URL arXiv:2310.01665
16. Gopal, A., Trefethen, L.: Solving laplace problems with corner singularities via rational functions. SIAM Journal of Numerical Analysis **57**(5), 2074–2094 (2019). URL https://doi.org/10.1137/19M125947X
17. Gopal, A., Trefethen, L.N.: New laplace and helmholtz solvers. Proceedings of the National Academy of Sciences **116**(21), 10223–10225 (2019). DOI 10.1073/pnas.1904139116. URL https://www.pnas.org/doi/abs/10.1073/pnas.1904139116
18. Greengard, L., Li, J.R.: On the numerical solution of the heat equation I: Fast solvers in free space. Journal of Computational Physics **226**, 1891–1901 (2007)
19. Gross, B., Kuberry, P., Atzberger, P.: First-passage time statistics on surfaces of general shape: Surface PDE solvers using Generalized Moving Least Squares (GMLS). Journal of Computational Physics **453**, 110932 (2022). DOI https://doi.org/10.1016/j.jcp.2021.110932. URL https://www.sciencedirect.com/science/article/pii/S0021999121008275
20. Herremans, A., Huybrechs, D., L.N., T.: Resolution of singularities by rational functions. SIAM Journal of Numerical Analysis **61**(6), 2580–2600 (2023). URL https://doi.org/10.1137/23M1551821
21. Hsiao, G.C., Saranen, J.: Boundary Integral Solution of the Two-dimensional Heat Equation. Mathematical Methods in the Applied Sciences **16**, 87–114 (1993)
22. Hwang, C.O., Mascagni, M.: Electrical capacitance of the unit cube. Journal of Applied Physics **95**(7), 3798–3802 (2004). DOI 10.1063/1.1664031. URL https://doi.org/10.1063/1.1664031
23. Hwang, C.O., Mascagni, M., Won, T.: Monte Carlo methods for computing the capacitance of the unit cube. Mathematics and Computers in Simulation **80**(6), 1089–1095 (2010)
24. Jiang, S., Greengard, L., Wang, S.: Efficient sum-of-exponentials approximations for the heat kernel and their applications. Advances in Computational Mathematics **41**(3), 529–551 (2015)
25. Katz, R.A., Pizer, S.M.: Untangling the blum medial axis transform. International Journal of Computer Vision **55**, 139–153 (2003)
26. Kress, R.: Linear Integral Equations. Applied Mathematical Sciences. Springer (1999)
27. Kropinski, M., Quaife, B.: Fast integral equation methods for Rothe's method applied to the isotropic heat equation. Computers and Mathematics with Applications **61**, 2436–2446 (2010)

28. Kurella, V., Tzou, J., Coombs, D., Ward, M.: Asymptotic Analysis of First Passage Time Problems Inspired by Ecology. Bulletin of Mathematical Biology **77**(1), 83–125 (2015)
29. Lawley, S.D., Lindsay, A.E., Miles, C.E.: Receptor Organization Determines the Limits of Single-Cell Source Location Detection. Physical Review Letters **125**(1), 018102 (2020)
30. Li, J.R., Greengard, L.: High order accurate methods for the evaluation of layer heat potentials. SIAM Journal on Scientific Computing **31**(5), 3847–3860 (2009)
31. Liesen, J., Sète, O., Nasser, M.M.S.: Fast and accurate computation of the logarithmic capacity of compact sets. Computational Methods and Function Theory **17**(4), 689–713 (2017)
32. Lindsay, A., Kolokolnikov, T., Tzou, J.: Narrow escape problem with a mixed trap and the effect of orientation. Physical Review E **91**, 032111 (2015). DOI 10.1103/PhysRevE.91.032111. URL https://link.aps.org/doi/10.1103/PhysRevE.91.032111
33. Lindsay, A.E.: An asymptotic study of blow up multiplicity in fourth order parabolic partial differential equations. Discrete and Continuous Dynamical Systems - B **19**(1), 189–215 (2014). DOI 10.3934/dcdsb.2014.19.189. URL https://www.aimsciences.org/article/id/4e4f5ce0-d5bc-4935-8089-741731a40690
34. Lindsay, A.E., Bernoff, A.J.: Kinetic Monte Carlo methods for three-dimensional diffusive capture problems in exterior domains. Royal Society Open Science **12**(2), 241033 (2025)
35. Lindsay, A.E., Bernoff, A.J., Navarro Hernández, A.: Short-time diffusive fluxes over membrane receptors yields the direction of a signalling source. Royal Society Open Science **10**(4), 221619 (2023)
36. Lindsay, A.E., Lega, J., Sayas, F.J.: The quenching set of a mems capacitor in two-dimensional geometries. Journal of Nonlinear Science **23**(5), 807–834 (2013)
37. Lindsay, A.E., Spoonmore, R., Tzou, J.: Hybrid asymptotic-numerical approach for estimating first passage time densities of the two- dimensional narrow capture problem. Physical Review E **94**, 042418 (2016)
38. Lindsay, A.E., Tzou, J.C., Kolokolnikov, T.: Optimization of First Passage Times by Multiple Cooperating Mobile Traps. SIAM Journal on Multiscale Modeling & Simulation **15**(2), 920–947 (2017). DOI 10.1137/16M1060169
39. Mauro, A.J., Sigurdsson, J.K., Shrake, J., Atzberger, P.J., Isaacson, S.A.: A First-Passage Kinetic Monte Carlo method for reaction–drift–diffusion processes. Journal of Computational Physics **259**, 536–567 (2014). DOI https://doi.org/10.1016/j.jcp.2013.12.023. URL https://www.sciencedirect.com/science/article/pii/S002199911300822X
40. Melnikov, Y.A., Reshniak, V.: A semi-analytical approach to Green's functions for heat equation in regions of irregular shape. Engineering Analysis with Boundary Elements **46**, 108–115 (2014)
41. Nakatsukasa, Y., Trefethen, L.N.: Reciprocal-log approximation and planar pde solvers. SIAM Journal on Numerical Analysis **59**(6), 2801–2822 (2021). DOI 10.1137/20M1369555
42. Plunkett, C.E., Lawley, S.D.: Boundary Homogenization for Partially Reactive Patches. SIAM Journal on Multiscale Modeling & Simulation **22**(2), 784–810 (2024). DOI 10.1137/23M1573422
43. Pólya, G., Szegő, G.: Isoperimetric Inequalities in Mathematical Physics, *Annals of Mathematics Studies*, vol. 27. Princeton University Press (1951). URL https://books.google.com/books?id=HWc8gFW2XXgC
44. Qiu, T., Rieder, A., S, F.S., Zhang, S.: Time-domain boundary integral equation modeling of heat transmission problems. Numerische Mathematik **143**, 223–259 (2019)
45. Schumm, R.D., Bressloff, P.C.: A numerical method for solving snapping out Brownian motion in 2D bounded domains. Journal of Computational Physics **493**, 112479 (2023)
46. Talbot, A.: The Accurate Numerical Inversion of Laplace Transforms. IMA Journal of Applied Mathematics **23**(1), 97–120 (1979)
47. Tausch, J.: A fast method for solving the heat equation by layer potentials. Journal of Computational Physics **224**, 956–969 (2007)
48. Trefethen, L.N.: Polynomial and rational convergence rates for laplace problems on planar domains. Proc. R. Soc. A **480** (2024). URL https://doi.org/10.1098/rspa.2024.0178
49. Trefethen, L.N., Weideman, J.A.C., Schmelzer, T.: Talbot Quadratures and Rational Approximations. BIT Numerical Mathematics **46**, 653–670 (2006)
50. Veeranpaneni, S., Biros, G.: A High-Order Solver for the Heat Equation in 1D domains with Moving Boundaries. SIAM Journal on Scientific Computing **29** (2006)
51. Ye, Y., Chaigneau, A., Grebenkov, D.S.: Escape-from-a-layer approach for simulating the boundary local time in euclidean domains. Journal of Computational Physics **537**, 114099 (2025). DOI https://doi.org/10.1016/j.jcp.2025.114099. URL https://www.sciencedirect.com/science/article/pii/S0021999125003821